Front. Phys.
https://doi.org/10.15302/frontphys.2026.115205
CN 11-5994/O4
ISSN 2095-0462

RESEARCH ARTICLE

Giant tunneling magnetoresistance in altermagnetic heterostructures via multi-stage spin-filtering

Fei Zou[1], Long Zhang[1], Jiangchao Han[2], Guoying Gao[1,3,*]

[1] School of Physics, Huazhong University of Science and Technology, Wuhan 430074, China
[2] Shanxi Key Laboratory of Artificial Intelligence & Micro Nano Sensors, College of Integrated Circuits, Taiyuan University of Technology, Taiyuan 030024, China
[3] Wuhan National High Magnetic Field Center, Huazhong University of Science and Technology, Wuhan 430074, China
Corresponding author. E-mail: guoying_gao@mail.hust.edu.cn
Received April 17, 2026; accepted May 30, 2026

ABSTRACT

Altermagnets, which combine the advantages of ferromagnetic spin splitting and antiferromagnetic zero stray field, have been regarded as a promising platform for spintronic applications. However, it is challenging to achieve high tunneling magnetoresistance (TMR) in altermagnet-based tunnel junctions due to the momentum-dependent spin splitting. By leveraging the intrinsic spin-dependent tunneling asymmetry of altermagnetic (AM) insulators, we investigate spin-polarized transport properties in altermagnetic tunnel junctions (AMTJs) with fully altermagnetic heterostructure barriers using first-principles quantum-transport calculations. Specifically, we design and compare [110]-oriented heterostructured AMTJs composed of $IrO_2/CoF_2/MF_2/CoF_2/IrO_2$ (M = Fe, Mn) with a homogeneous CoF_2-barrier reference. Our results show that the FeF_2-based heterostructure achieves giant TMR ratios of up to 196,468%, while the MnF_2-based counterpart yields substantial values up to 2,322%, far exceeding the modest 14% obtained for the homogeneous CoF_2 barrier system. Mechanistically, this enhancement originates from a multi-stage spin-filtering effect enabled by the heterostructured barriers, which breaks the single transport-mode constraint of homogeneous barriers through the symmetry-selective superposition of spin states. These findings highlight the potential of staggered altermagnetic heterostructures to overcome the single-mode transport limitation of conventional MTJs, providing a robust pathway toward next-generation high-performance altermagnetic spintronic devices.

Keywords altermagnet, tunnel junction, spin filtering, first-principles calculations

Just Accepted

This is a “Just Accepted” manuscript, which has been examined by the peer-review process and has been accepted for publication. A “Just Accepted” manuscript is published online shortly after its acceptance, which is prior to technical editing and formatting and author proofing. Higher Education Press (HEP) provides “Just Accepted” as an optional and free service which allows authors to make their results available to the research community as soon as possible after acceptance. After a manuscript has been technically edited and formatted,

RESEARCH ARTICLE

Giant tunneling magnetoresistance in altermagnetic heterostructures via multi-stage spin-filtering

Fei Zou[1], Long Zhang[1], Jiangchao Han[2], Guoying Gao[1,3,*]

[1] School of Physics, Huazhong University of Science and Technology, Wuhan 430074, China

[2] Shanxi Key Laboratory of Artificial Intelligence & Micro Nano Sensors, College of Integrated Circuits, Taiyuan University of Technology, Taiyuan 030024, China

[3] Wuhan National High Magnetic Field Center, Huazhong University of Science and Technology, Wuhan 430074, China

Corresponding author. E-mail: [†]guoying_gao@mail.hust.edu.cn

Received April 17, 2026; accepted May 30, 2026

ABSTRACT

Altermagnets, which combine the advantages of ferromagnetic spin splitting and antiferromagnetic zero stray field, have been regarded as a promising platform for spintronic applications. However, it is challenging to achieve high tunneling magnetoresistance (TMR) in altermagnet-based tunnel junctions due to the momentum-dependent spin splitting. By leveraging the intrinsic spin-dependent tunneling asymmetry of altermagnetic (AM) insulators, we investigate spin-polarized transport properties in altermagnetic tunnel junctions (AMTJs) with fully altermagnetic heterostructure barriers using first-principles quantum-transport calculations. Specifically, we design and compare [110]-oriented heterostructured AMTJs composed of $IrO_2/CoF_2/MF_2/CoF_2/IrO_2$ (M = Fe, Mn) with a homogeneous CoF_2-barrier reference. Our results show that the FeF_2-based heterostructure achieves giant TMR ratios of up to 196,468%, while the MnF_2-based counterpart yields substantial values up to 2,322%, far exceeding the modest 14% obtained for the homogeneous CoF_2 barrier system. Mechanistically, this enhancement originates from a multi-stage spin-filtering effect enabled by the heterostructured barriers, which breaks the single transport-mode constraint of homogeneous barriers through the symmetry-selective superposition of spin states. These findings highlight the potential of staggered altermagnetic heterostructures to overcome the single-mode transport limitation of conventional MTJs, providing a robust pathway toward next-generation high-performance altermagnetic spintronic devices.

Keywords altermagnet, tunnel junction, spin filtering, first-principles calculations

1 Introduction

Magnetic tunnel junctions (MTJs), comprising two magnetic electrodes separated by an insulating barrier, are central elements in spin-based information technologies [1, 2]. Their operation relies on tunneling magnetoresistance (TMR), whereby spin-dependent quantum tunneling becomes sensitive to the relative orientation of the electrode magnetizations, enabling nonvolatile memory, magnetic sensing, and logic functionalities [3–6]. Conventional MTJs employ spin-polarized ferromagnetic (FM) electrodes, such as

Fe/MgO/Fe junction and recently proposed van der Waals MTJs based on graphene/h-BN and $\alpha-In_2Se_3$ [7–9]. However, FM-based architectures face intrinsic limitations, including stray fields, scaling challenges associated with magnetostatic coupling, and thermal instability in nanoscale devices [10–13]. By contrast, Antiferromagnets (AFMs) offer zero net magnetization, absence of stray fields, and ultrafast dynamics, yet their compensated spin structure generally yields zero spin polarization, limiting their effectiveness in tunneling devices [14, 15]. These constraints highlight the need for magnetic materials that combine the advantages of AFMs with robust spin-dependent electronic structure.

Recently, altermagnets (AMs) have attracted extensive interest as a distinct class of compensated magnets in which opposite spin sublattices give rise to large, symmetry-protected, momentum-dependent spin splitting even in the absence of spin–orbit coupling (SOC) [16–20]. Their alternating spin polarization—manifested simultaneously in real space through the crystal sublattices and in momentum space through the band structure—arises despite possessing zero net magnetization. Representative materials include collinear AMs such as CrSb [21], MnTe [22], RuO_2 [23], the transition-metal difluorides XF_2 (X = Co, Fe, Mn) [24–27], and MnS_2 [28]. By effectively combining the key advantages of both FMs and AFMs, the unique properties of AMs have stimulated extensive theoretical and experimental efforts aimed at predicting novel spin-transport phenomena in AM-based MTJs (AMTJs) [28–36]. In AMTJs with ordinary insulating barriers, AM metals serve as functional electrodes. By employing either symmetric dual-AM metallic electrodes or asymmetric combinations of a single AM electrode with other metals, the momentum-space spin splitting of altermagnets can be harnessed to serve as an efficient source of spin-polarized electrons [30, 33, 36–41]. Alternatively, in AMTJs with altermagnetic barriers, AM insulators act as both tunnel barriers and active spin-filtering media [34, 35, 43]. Building upon these concepts, research has expanded toward integrated multilayered architectures, ranging from AM heterostructure barriers separated by non-magnetic spacers—such as $Ag/V_2Te_2O/BiOCl/V_2Te_2O/Ag$ [42] —to fully altermagnetic MTJs, exemplified by the $RuO_2/NiF_2/RuO_2$ [43] system. In these configurations, AMs exhibit a dual physical role: providing highly polarized carrier injection as electrodes or active magnetic layers, and enabling precise spin-selective tunneling as barriers through spin-dependent wave-function decay. These architectures exploit the unique spin-polarized electronic structures of AMs, offering new degrees of freedom to overcome the performance limitations of conventional MTJs.

In addition, the spin-transport properties of AM-based MTJs are inherently orientation-dependent due to the momentum-space spin splitting characteristic of AMs [33–35, 40]. The anisotropic Fermi surfaces in AM metallic electrodes determine the spin polarization of propagating states, so the injected carrier spin polarization, symmetry filtering, and momentum-resolved transmission channels depend on the transport direction. Similarly, the altermagnetic insulating barriers project distinct regions of their spin-dependent complex band structures onto the two-dimensional Brillouin zone. Therefore, changing the crystallographic orientation (e.g., [001] versus [110]) fundamentally alters the symmetry-filtering rules and the decay rates of evanescent states within the altermagnetic insulator (AMI). Recent studies have shown that the evanescent states in FeF_2 exhibit pronounced spin polarization along the [110] direction, leading to more efficient spin-selective transport than along the [001] direction [35].

This orientation-sensitive tunneling mechanism leads to markedly different spin-selective efficiencies, suggesting that the performance of AM-based MTJs can be precisely engineered through the synergistic alignment of electrode injection and barrier filtering. Here, we specifically focus on the optimization of the barrier filtering stage. While previous studies have primarily explored MTJ designs employing either a single AMI layer [34, 35] or an AM/M/AM heterostructure (where M represents a nonmagnetic insulator) [26, 42], the potential of utilizing a fully altermagnetic heterostructure as a tunnel barrier remains unexplored. Such an architecture, particularly along the [110] direction, offers a unique opportunity to exploit the distinct spin-dependent decay characteristics of different AMIs to achieve multi-stage spin modulation.

In this work, leveraging the intrinsic spin-dependent tunneling asymmetry of the AMIs CoF_2(110), FeF_2(110), and MnF_2(110), we design and compare [110]-oriented heterostructured AMTJs composed of $IrO_2/CoF_2/MF_2/CoF_2/IrO_2$ (M = Fe, Mn) with a homogeneous CoF_2-barrier reference. These architectures integrate nonmagnetic metallic IrO_2 electrodes and a full altermagnetic insulating tunneling barrier composed of either $CoF_2/FeF_2/CoF_2$ or $CoF_2/MnF_2/CoF_2$. For comparison, the reference junction employs a single-material $CoF_2/CoF_2/CoF_2$ barrier without heterostructure modulation. First-principles quantum-transport simulations show that, even without half-metallic electrodes, the former structure achieves giant TMR ratios of 134,202% and 196,468%, whereas the latter yields substantial values of 550% and 2,322%, far exceeding the modest 79% and 14% obtained for the single-material CoF_2 barrier system. The excellent TMR effect is attributed to the multi-stage spin-filtering effect enabled by the heterostructured barriers. The resulting symmetry-selective superposition of spin states significantly enhances the overall tunneling spin-selectivity of the device. Together, these considerations indicate that the proposed AM-based MTJs represent a promising new platform for investigating momentum-dependent symmetry-driven spin-filtering mechanisms and for realizing high-performance and high-density spintronic devices.

2 Computational methods

First-principles calculations were performed within the framework of density functional theory (DFT) using the Vienna Ab initio Simulation Package (VASP) [44]. The pseudopotentials were described by the projector-augmented-wave method, and the generalized gradient approximation (GGA) of Perdew-Burke-Ernzerhof (PBE) [45] exchange-correlation functional was employed. The cutoff energy was set to 500 eV. For all bulk materials, structural relaxation was performed using a k-point mesh of 12×12×16. The calculations were continued until the total energy difference and the maximum ionic forces converged to below 10^{-6} eV and 0.001 eV/Å, respectively. Electronic structures were calculated using the GGA+U method [46], with U_{eff} values of 6.0 eV (Co/Fe *3d* electrons) and 5.5 eV (Mn *3d* electrons). The relaxed lattice constants are a = b = 4.707 Å and c = 3.203 Å for CoF_2; a = b = 4.716 Å and c = 3.345 Å for FeF_2; a = b = 4.904 Å and c = 3.313 Å for MnF_2; and a = b = 4.538 Å and c = 3.189 Å for IrO_2, in agreement with the experimental or theoretical values [24, 47−49]. For all tunnel junctions, a 20-Å-thick vacuum was added to separate the periodic superlattice. The in-plane lattice constants of these MTJs were fixed to those of bulk CoF_2(110) i.e. a = 3.203 Å and b = 6.657 Å. Given these MTJ lattice constants, the lattice

mismatch of the other three materials relative to CoF_2(110) was less than 5%. A k-point mesh of 10×5×1 was used to relax the atomic coordinates of the AMTJs. The energy-convergence criterion was set to 10^{-5} eV, and the atomic positions were optimized until the forces on each atom were less than 0.02 eV/Å.

The transport properties of the AMTJs were calculated using DFT combined with the nonequilibrium Green's function (NEGF) formalism as implemented in QuantumATK [50], which has been used in our recent works on altermagnetic tunnel junctions [36, 43]. The exchange–correlation potential was described using the PBE-based spin-polarized GGA+*U* method [45, 51], together with a double-zeta-polarized (DZP) basis set. The effective *U* values (U_{eff}) for the Co, Fe, and Mn 3d orbitals were set to 4.5, 5.0, and 4.0 eV, respectively. A cutoff energy of 150 Ha and a 16×8×150 k-point mesh were used for the AMTJs. Transmission functions were calculated using a 401×401 k-point mesh in the two-dimensional (2D) Brillouin zone of the devices. We tested a range of U_{eff} values for Co, Fe, and Mn based on previous theoretical studies of CoF_2, FeF_2 and MnF_2. The selected U_{eff} parameters in QuantumATK yield band gaps for CoF_2, FeF_2 and MnF_2 that are in good agreement with our VASP results as well as previously reported values [24, 26, 35].

3 Results and discussion

AMIs exhibit nonrelativistic spin splitting in momentum space, giving rise to spin-polarized tunneling along crystallographic directions corresponding to the split reciprocal-space paths [24–27]. Electron tunneling through conventional insulating barriers (e.g., TiO_2 and MgO) is spin-degenerate, whereas an altermagnetic insulating barrier lifts this degeneracy, endowing AMTJs with intrinsic spin selectivity and expanded tunability of transport properties, thereby enhancing device performance [26, 34, 35, 43]. Here, we investigate the role of the tunnel barrier in AMTJs by designing a heterostructure composed of three altermagnetic insulating layers arranged in an ABA-type configuration using two distinct AMI materials, as illustrated in Fig. 1. To isolate the intrinsic spin-dependent transport arising solely from the barrier, nonmagnetic metal electrodes with no spin polarization are employed. This AMTJ operates based on the spin-selective tunneling asymmetry between the two types of AMI barriers (denoted AMI-A and AMI-B), which governs the transmission probability. The relative Néel vector orientations of the barrier layers introduce three controllable magnetic degrees of freedom for switching, namely the P (parallel) state with all Néel vectors aligned parallel, the AP (antiparallel)-I state in which the Néel vector of the rightmost barrier (AMI-A) is reversed, and the AP-II state where the Néel vector of the central barrier (AMI-B) is reversed. Experimentally, such magnetic configurations may be manipulated through exchange bias, external magnetic fields, or current-induced spin-orbit torques, as demonstrated in previous antiferromagnetic spintronic studies [31, 52-54]. This architecture eliminates the reliance on ferromagnetic electrodes, thereby suppressing stray fields and improving spin-dynamical stability.

Rutile-type MF_2 (M = Co, Fe, Mn) are insulating compounds that have recently been proposed as AMs [24–27, 55–57]. Their crystal structures, magnetic configurations, and electronic band structures are shown in Fig. 2. The calculated magnetic moments at the Co, Fe, and Mn sites (2.77, 3.79, and 4.60 μ_B) and band gaps (4.34, 3.49, and 3.94 eV) for CoF_2, FeF_2 and MnF_2 agree well with reported theoretical and experimental values [24, 35, 47,

57]. The band structures of CoF_2, FeF_2, and MnF_2 exhibit pronounced spin splitting along the high-symmetry Γ–M and A–Z paths in reciprocal space [Figs. 2(c, e)]. The valence-band spin splitting at the Γ–M path reaches 0.43, 0.08, and 0.04 eV for CoF_2, FeF_2, and MnF_2, respectively, consistent with previous reports and indicative of their altermagnetic nature [26, 34]. Spin splitting is observed along the Γ–M path of MF_2 (001) and the Γ–X path of MF_2 (110) [Figs. 2(f)–(h)], implying that electron tunneling along the [110] crystallographic direction becomes spin-polarized, thereby generating spin-polarized currents analogous to those in FMs. Furthermore, the lowest decay rates of the evanescent states reveal globally spin-polarized tunneling along the [110] direction [35]. In contrast, the bands remain spin-degenerate along the Γ–Z direction, and therefore the transport properties along [110] are the focus of this work. To evaluate the TMR performance of the proposed AMTJ architecture [Fig. 1], we investigate and compare heterostructured AMTJs composed of $IrO_2/CoF_2/MF_2/CoF_2/IrO_2$ (M = Fe, Mn) with a homogeneous CoF_2 barrier reference. In the heterostructured configurations, one unit cell (UC) of CoF_2 is used for each outer barrier layer (corresponding to the AMI-A regions in Fig. 1), while one UC of FeF_2(110) or MnF_2(110) serves as the central barrier layer (AMI-B region). Conversely, in the homogeneous reference, one UC of CoF_2(110) is employed for all three barrier layers, representing both the AMI-A and AMI-B regions. The electrodes are made of nonmagnetic metallic IrO_2(110), whose electronic structure and conduction channels are shown in Fig. S1.

The investigation begins with the IrO_2(110)/CoF_2/FeF_2/CoF_2/IrO_2 AMTJ. Figure 3(a) depicts its atomic structure and magnetic configuration of the AMTJ in the P state. The transitions from the P state to the AP-I and AP-II states define the magnetoresistance ratios TMR-I and TMR-II, respectively. The TMR is defined as $TMR = abs(T_P\text{-}T_{AP})/min(T_P,T_{AP})\times100\%$, where T_P and T_{AP} denote the transmission coefficients for P and AP magnetization alignments, respectively. Figures 3(b), (c), and (m) show the spin-resolved and total transmission coefficients, as well as the TMR ratios, as functions of energy. At the Fermi level, the TMR-I and TMR-II ratios reach as high as 134,202% and 196,468%, respectively, far exceeding the previously reported value of 3,956% in CrO_2(110)/FeF_2/IrO_2 junction based on a half-metallic electrode [35]. Such extraordinarily large TMR ratios enable significantly enhanced signal contrast and hold strong potential for high-performance spintronic memory and sensing applications. Moreover, the device maintains TMR values exceeding 1,000% over multiple energy points. In the energy range below the Fermi level, TMR-II remains above 300% at most energies, while in a finite window above the Fermi level, TMR-I exceeds 200% across nearly the entire energy range, demonstrating robust and broadband spin-dependent transport characteristics. A giant TMR without the use of half-metallic electrodes indicates that the TMR originates from robust intrinsic spin filtering and symmetry-driven spin selectivity, which ensure extremely high readout contrast and superior sensitivity to magnetic state variations.

The TMR performance of the AMTJ is strongly governed by the spin polarization of the tunneling electrons. The spin-filtering efficiency (SFE) is calculated as $SFE=(T_\uparrow\text{-}T_\downarrow)/(T_\uparrow+T_\downarrow)\times100\%$, where $T_\uparrow$ and $T_\downarrow$ denote the spin-resolved transmission coefficients at the Fermi energy. Figures 3(d)–3(i) display the spin- and $\vec{k}_{||}$-resolved transmission spectra in momentum space for the AMTJ. The $\vec{k}_{||}$-resolved spin-filtering efficiency $SFE(\vec{k}_{||})$ is

shown in Figs. 3(j)–(l). At the Fermi level, the spin-down channel dominates the tunneling transport in the P configuration, with a transmission coefficient much larger than that of the spin-up channel [Fig. 3(b)]. In the $\vec{k}_{||}$ space, most regions exhibit nearly −100% spin filtering [Figs. 3(d, e, j)], resulting in a SFE approaching −100%. When the magnetic configuration switches to the AP-I, the SFE decreases to approximately −96%, which originates from an increase in spin-up transmission accompanied by a reduction in spin-down transmission [Figs. 3(b, f, g, k)]. Upon further switching to the AP-II configuration, the spin-up transmission exceeds the spin-down component [Figs. 3(b, h, i, l)], leading to a positive SFE of about 63%. It is worth noting that the spatial distribution of the transmission spectrum in the $\vec{k}_{||}$ plane shows a certain resemblance to that of the electrode conducting channels [Fig. S1(c)]. However, for this AMTJ, the electrode channels are not the dominant factor governing the tunneling amplitude in the tunneling process. The SFE reaching 100% in the P configuration indicates that the dominant mechanism of tunneling originates from the spin-selective transmission of the barrier layers, whereas the interfacial band-symmetry matching plays only a secondary and modulating role. The electrodes primarily serve to provide propagating states in the corresponding $\vec{k}_{||}$ regions that can couple to the barrier states, rather than fundamentally determining the transmission magnitude. Specifically, in the P configuration, spin-down electrons exhibit markedly enhanced transmission in the bright purple arc-like regions on both sides of the Y–Γ–Y' path, forming dominant tunneling channels that contribute most of the total transmission. This feature suggests an efficient coupling between the electrode states in these $\vec{k}_{||}$ regions and the lowest decay rates of the evanescent states in the barrier. When the magnetic configuration switches to AP-I or AP-II, the spin-selective transmission characteristics of the middle and right barrier layers are altered. As a consequence, the dominant tunneling channels present in the P state are effectively suppressed. This leads to a strong reduction of the tunneling probability for spin-down electrons at the Fermi level, and the total transmission decreases by approximately three orders of magnitude compared with the P state [Fig. 3(c)]. The blockage of tunneling channels induced by the change in spin selectivity of the barrier layers is therefore the direct physical origin of the giant TMR.

The spin- and layer-resolved projected device density of states (PDDOS) (Fig. 4) further corroborates the interpretation derived from transport calculations. The left IrO_2 electrode is defined as the electron source. In the P configuration [Fig. 4(a)], the spin-down PDDOS near the Fermi level in the right electrode region is substantially larger than the spin-up component, confirming that tunneling is dominated by spin-down electrons and demonstrating the strong filtering of spin-up carriers in this state. The overall density of states (DOS) in the P configuration is also higher than those in the AP-I and AP-II states, consistent with the physical origin of the giant TMR. In contrast, in the AP-I configuration, the spin-down states near the Fermi level are markedly suppressed [Fig. 4(b)]. This reduction arises because reversing the Néel vector of the right barrier layer blocks the highly transmissive spin-down tunneling channels. For the AP-II configuration, the spin-up and spin-down PDDOS components become comparable near the Fermi level [Fig. 4(c)]. This behavior indicates that efficient tunneling channels for both spin species are largely closed, which explains the reduced spin polarization observed in the AP-

II state.

For the IrO_2(110)/CoF_2/MnF_2/CoF_2/IrO_2 AMTJ, the spin-resolved transmission coefficients, total transmission coefficients, and TMR ratios as functions of energy are shown in Figs. 5(a)–(c). In the P configuration, the total transmission of the system remains the largest, and transport near the Fermi level is still dominated by the spin-down channel. The calculated TMR values at the Fermi level reach 550% (TMR-I) and 2,322% (TMR-II), significantly exceeding the 150−170% range reported for the NM/CoF_2/NI/CoF_2/NM junction (where NM and NI denote a normal metal and a normal insulator, respectively) [26]. Nevertheless, these TMR values are significantly smaller than those of the FeF_2-based AMTJ discussed above. This reduction originates from weaker spin-down tunneling in the P state, reflecting less efficient matching of the slowest-decaying evanescent states in the MnF_2 barrier with those in CoF_2 compared with the FeF_2/CoF_2 case, which partially suppresses the highly transmissive spin-down channels and thereby limits the overall TMR. Consistently, the spin-down transmission spectrum in the P configuration [Figs. S2(a)–(f)] does not exhibit the bright arc-like features along Y–Γ–Y' seen in the FeF_2-based AMTJ. Instead, the main contribution to the total transmission arises from tunneling channels near the C and C' regions [Fig. S2(b)], whose contribution is noticeably smaller than that of the arc-like channels in the FeF_2-based AMTJ. When the magnetic configuration switches to AP-I or AP-II, the efficient tunneling channels for both spin species are largely closed, suppressing electron transmission at the Fermi level and reducing the total conductance. This channel blocking leads to the sizable TMR observed in these configurations. The corresponding $\vec{k}_{||}$-resolved SFE maps are shown in Figs. S3(g)–(i), yielding SFE values of −98% (P), −95% (AP-I), and −22% (AP-II). The overall spin-filtering effect is therefore weaker than that in the FeF_2-based AMTJ for the corresponding magnetic states.

To further elucidate the physical origin of the observed giant TMR, we investigated a reference AMTJ with a homogeneous tunneling barrier—specifically the IrO_2(110)/CoF_2/CoF_2/CoF_2/IrO_2 structure. By eliminating internal material interfaces within the barrier region, this configuration serves as an ideal reference to isolate the intrinsic transport properties of a single altermagnetic phase from the multi-stage filtering effects. The spin-resolved transmission coefficients, total transmission spectra, and TMR ratios as a function of energy are shown in Figs. 5(d, e, f). Although the spin-down tunneling remains stronger than the spin-up contribution, the total transmission is no longer maximized in the P configuration but instead in the AP-I state. At the Fermi level, the transmission coefficients of all magnetic configurations are comparable, yielding modest TMR values of 79% (TMR-I) and 14% (TMR-II), indicating an almost negligible magnetoresistance effect. Several energy points slightly below the Fermi level show enhanced TMR, and TMR-I stabilizes around ~200% above the Fermi level. The low TMR at the Fermi level indicates weak SFE in this system. The corresponding $\vec{k}_{||}$-resolved SFE maps are presented in Figs. S3(g)–(i), giving SFE values of −80% (P), −88% (AP-I), and −47% (AP-II), indicative of only moderate spin-filtering capability. This suggests that the spin-selective tunneling characteristics of the barrier do not differ substantially among the various configurations, preventing the formation of a sufficiently large conductance contrast and thereby limiting the overall magnetoresistance effect. The modest TMR values (79% and

14%) suggest that a homogeneous CoF_2 barrier provides only a single stage of symmetry filtering. Without the modulation of an additional altermagnetic phase, the evanescent states of the minority spin are not sufficiently suppressed across the entire barrier thickness, failing to achieve the near-complete spin-selectivity required for giant magnetoresistance.

The remarkable enhancement in TMR ratios originates from a multi-stage spin-filtering mechanism. In the single-material CoF_2 barrier, spin selection is limited by the intrinsic filtering capacity of a single complex band structure. In contrast, the $CoF_2/FeF_2/CoF_2$ heterostructure functions as a series of specialized filters. Since CoF_2 and FeF_2 possess distinct spin-split projections in momentum space, their interleaved arrangement sequentially suppresses residual leakage from non-targeted spin channels, leading to a much higher cumulative spin-selectivity than a homogeneous CoF_2 barrier. Along the [110] direction, the selective superposition of evanescent states plays a critical role. The giant TMR in the FeF_2-based AMTJ suggests that the [110] oriented evanescent states of CoF_2 and FeF_2 exhibit highly compatible symmetry for the majority spin, while maintaining a drastic decay rate disparity for the minority spin. This synergistic superposition strongly promotes conductance in the P configuration while suppressing it in the AP-I and AP-II configurations, thereby maximizing the TMR ratios. The performance gap between the FeF_2 (196,468%) and MnF_2 (2,322%) systems originates from the different decay characteristics of their evanescent states. In the MnF_2 system, the evanescent states may exhibit insufficient decay contrast or partial momentum-space overlap with the leakage channels of CoF_2. Ultimately, the heterostructure architecture breaks the single-transport-mode limitation of homogeneous barriers. By introducing altermagnetic interfaces, the device utilizes coherent tunneling modulation to reshape the spin-polarized evanescent potentials across different layers. This provided degree of freedom allows for the precise manipulation of tunneling probabilities through the staggered decay constants of different altermagnets—a mechanism fundamentally unavailable in single-barrier $IrO_2(110)/CoF_2/IrO_2$ structures.

4 Conclusions

In conclusion, leveraging the intrinsic spin-dependent tunneling asymmetry of the altermagnetic insulators $CoF_2(110)$, $FeF_2(110)$, and $MnF_2(110)$, we have designed and compared [110]-oriented heterostructured AMTJs composed of $IrO_2/CoF_2/MF_2/CoF_2/IrO_2$ (M = Fe, Mn) with a homogeneous CoF_2-barrier reference. First-principles quantum-transport simulations show that, even without half-metallic electrodes, the FeF_2-based AMTJ achieves giant TMR ratios of 134,202% and 196,468%, whereas the MnF_2-based one yields substantial values of 550% and 2,322%, far exceeding the modest 79% and 14% obtained for the single-material CoF_2 barrier system. Mechanistically, these results are attributed to the multi-stage spin-filtering effect enabled by the heterostructured barriers ($CoF_2/FeF_2/CoF_2$ and $CoF_2/MnF_2/CoF_2$). This architecture breaks the single transport mode constraint of homogeneous barriers by utilizing the distinct spin-polarized tunneling modulations of different magnetic layers. The resulting symmetry-selective superposition of spin states significantly enhances the overall tunneling spin-selectivity of the device. Furthermore, as these AMTJs are composed of altermagnetic and non-magnetic materials, they effectively eliminate stray magnetic fields and magnetic crosstalk. This ensures high integration density and

robust stability against external perturbations. Consequently, MTJs employing altermagnetic heterostructure barriers offer superior signal contrast and higher performance for spintronic memory and sensing applications, providing a novel paradigm for the design of next-generation MTJ devices.

Declarations The authors declare that they have no competing interests and there are no conflicts.

Electronic supplementary materials The online version contains supplementary material available at https://doi.org/10.15302/frontphys.2026.115205.

Acknowledgements This work was supported by the National Natural Science Foundation of China (Grant No. 12174127).

References

1. M. Julliere, Tunneling between ferromagnetic films, *Phys. Lett. A* 54(3), 225 (1975) https://doi.org/10.1016/0375-9601(75)90174-7

2. J. S. Moodera, L. R. Kinder, T. M. Wong, and R. Meservey, Large magnetoresistance at room temperature in ferromagnetic thin film tunnel junctions, *Phys. Rev. Lett.* 74(16), 3273 (1995) https://doi.org/10.1103/PhysRevLett.74.3273

3. S. A. Wolf, D. D. Awschalom, R. A. Buhrman, J. M. Daughton, S. von Molnár, M. L. Roukes, A. Y. Chtchelkanova, and D. M. Treger, Spintronics: a spin-based electronics vision for the future, *Science* 294(5546), 1488 (2001) https://doi.org/10.1126/science.1065389

4. E. Y. Tsymbal, O. N. Mryasov, and P. R. LeClair, Spin-dependent tunnelling in magnetic tunnel junctions, *J. Phys.: Condens. Matter* 15(4), R109 (2003) https://doi.org/10.1088/0953-8984/15/4/201

5. I. Žutić, J. Fabian, and S. Das Sarma, Spintronics: Fundamentals and applications, *Rev. Mod. Phys.* 76(2), 323 (2004) https://doi.org/10.1103/RevModPhys.76.323

6. J. Lenz and S. Edelstein, Magnetic sensors and their applications, *IEEE Sens. J.* 6(3), 631 (2006) https://doi.org/10.1109/JSEN.2006.874493

7. S. Yuasa, T. Nagahama, A. Fukushima, Y. Suzuki, and K. Ando, Giant room-temperature magnetoresistance in single-crystal Fe/MgO/Fe magnetic tunnel junctions, *Nat. Mater.* 3(12), 868 (2004) https://doi.org/10.1038/nmat1257

8. Z. Yan, J. Xiao, X. Zhang, C. Fang, and X. Xu, Giant tunneling magnetoresistance in Mn- and V-intercalated graphene/h-BN Based van der Waals magnetic tunnel junctions, *Adv. Funct. Mater.* 36(15), e11719 (2026) https://doi.org/10.1002/adfm.202511719

9. Z. Yan, Z. Li, Y. Han, Z. Qiao, and X. Xu, Giant tunneling magnetoresistance and electroresistance in α−In_2Se_3-based van der Waals multiferroic tunnel junctions, *Phys. Rev. B* 105(7), 075423 (2022) https://doi.org/10.1103/PhysRevB.105.075423

10. A. Hirohata, K. Yamada, Y. Nakatani, I. L. Prejbeanu, B. Diény, P. Pirro, and B. Hillebrands, Review on spintronics: Principles and device applications, *J. Magn. Magn. Mater.* 509, 166711 (2020) https://doi.org/10.1016/j.jmmm.2020.166711

11. V. D. Nguyen, S. Rao, K. Wostyn, and S. Couet, Recent progress in spin-orbit torque magnetic random-access memory, *npj Spintronics* 2(1), 48 (2024) https://doi.org/10.1038/s44306-024-00044-1

12. D. Weller and A. Moser, Thermal effect limits in ultrahigh-density magnetic recording, *IEEE Trans. Magn.* 35(6), 4423 (1999) https://doi.org/10.1109/20.809134

13. T. Jungwirth, X. Marti, P. Wadley, and J. Wunderlich, Antiferromagnetic spintronics, *Nat. Nanotechnol.* 11(3), 231 (2016) https://doi.org/10.1038/nnano.2016.18

14. V. Baltz, A. Manchon, M. Tsoi, T. Moriyama, T. Ono, and Y. Tserkovnyak, Antiferromagnetic spintronics, *Rev. Mod. Phys.* 90(1), 015005 (2018) https://doi.org/10.1103/RevModPhys.90.015005

15. S. A. Siddiqui, J. Sklenar, K. Kang, M. J. Gilbert, A. Schleife, N. Mason, and A. Hoffmann, Metallic antiferromagnets, *J. Appl. Phys.* 128(4), 040904 (2020) https://doi.org/10.1063/5.0009445

16. L. Šmejkal, J. Sinova, and T. Jungwirth, Beyond conventional ferromagnetism and antiferromagnetism: A phase with nonrelativistic spin and crystal rotation symmetry, *Phys. Rev. X* 12(3), 031042 (2022) https://doi.org/10.1103/PhysRevX.12.031042

17. S. Zeng, D. Liu, H. Peng, C. C. He, X. B. Yang, and Y. J. Zhao, Classification and design of two-dimensional altermagnets, *Front. Phys. (Beijing)* 21(9), 095301 (2026) https://doi.org/10.15302/frontphys.2026.095301

18. C. Song, H. Bai, Z. Zhou, L. Han, H. Reichlova, J. H. Dil, J. Liu, X. Chen, and F. Pan, Altermagnets as a new class of functional materials, *Nat. Rev. Mater.* 10(6), 473 (2025) https://doi.org/10.1038/s41578-025-00779-1

19. Z. Guo, X. Wang, W. Wang, G. Zhang, X. Zhou, and Z. Cheng, Spin-polarized antiferromagnets for spintronics, *Adv. Mater.* 37(36), 2505779 (2025) https://doi.org/10.1002/adma.202505779

20. W. Sun, C. Yang, W. Wang, Y. Liu, X. Wang, S. Huang, and Z. Cheng, Proposing altermagnetic-ferroelectric type-III multiferroics with robust magnetoelectric coupling, *Adv. Mater.* 37(26), 2502575 (2025) https://doi.org/10.1002/adma.202502575

21. J. Ding, Z. Jiang, X. Chen, Z. Tao, Z. Liu, T. Li, J. Liu, J. Sun, J. Cheng, J. Liu, Y. Yang, R. Zhang, L. Deng, W. Jing, Y. Huang, Y. Shi, M. Ye, S. Qiao, Y. Wang, Y. Guo, D. Feng, and D. Shen, Large band splitting in *g*-wave altermagnet CrSb, *Phys. Rev. Lett.* 133(20), 206401 (2024) https://doi.org/10.1103/PhysRevLett.133.206401

22. T. Osumi, S. Souma, T. Aoyama, K. Yamauchi, A. Honma, K. Nakayama, T. Takahashi, K. Ohgushi, and T. Sato, Observation of a giant band splitting in altermagnetic MnTe, *Phys. Rev. B* 109(11), 115102 (2024) https://doi.org/10.1103/PhysRevB.109.115102

23. T. Berlijn, P. C. Snijders, O. Delaire, H. D. Zhou, T. A. Maier, H. B. Cao, S. X. Chi, M. Matsuda, Y. Wang, M. R. Koehler, P. R. C. Kent, and H. H. Weitering, Itinerant antiferromagnetism in RuO_2, *Phys. Rev. Lett.* 118(7), 077201 (2017) https://doi.org/10.1103/PhysRevLett.118.077201

24. L. D. Yuan, Z. Wang, J. W. Luo, E. I. Rashba, and A. Zunger, Giant momentum-dependent spin splitting in centrosymmetric low-*Z* antiferromagnets, *Phys. Rev. B* 102(1), 014422 (2020) https://doi.org/10.1103/PhysRevB.102.014422

25. Y. Guo, H. Liu, O. Janson, I. C. Fulga, J. Van Den Brink, and J. I. Facio, Spin-split collinear antiferromagnets: A large-scale ab-initio study, *Mater. Today Phys.* 32, 100991 (2023) https://doi.org/10.1016/j.mtphys.2023.100991

26. K. Samanta, D. F. Shao, and E. Y. Tsymbal, Spin filtering with insulating altermagnets, *Nano Lett.* 25(8), 3150 (2025) https://doi.org/10.1021/acs.nanolett.4c05672

27. J. Sears, V. O. Garlea, D. Lederman, J. M. Tranquada, and I. A. Zaliznyak, Altermagnetic and dipolar splitting of magnons in FeF_2, arXiv: 2601.04303 (2026)

28. J. Wang, X. Yang, Z. Yang, J. Lu, P. Ho, W. Wang, Y. S. Ang, Z. Cheng, and S. Fang, Pentagonal 2D altermagnets: material screening and altermagnetic tunneling junction device application, *Adv. Funct. Mater.* 35, 2505145 (2025)

29. X. Yang, S. Fang, Z. Yang, P. Ho, J. Lu, and Y. S. Ang, Altermagnetic flatband‐driven fermi surface geometry for giant tunneling magnetoresistance, *Adv. Funct. Mater.* 36(35), e31921 (2026) https://doi.org/10.1002/adfm.202531921

30. D. F. Shao, S. H. Zhang, M. Li, C. B. Eom, and E. Y. Tsymbal, Spin-neutral currents for spintronics, *Nat. Commun.* 12(1), 7061 (2021) https://doi.org/10.1038/s41467-021-26915-3

31. P. Qin, H. Yan, X. Wang, H. Chen, Z. Meng, J. Dong, M. Zhu, J. Cai, Z. Feng, X. Zhou, L. Liu, T. Zhang, Z. Zeng, J. Zhang, C. Jiang, and Z. Liu, Room-temperature magnetoresistance in an all-antiferromagnetic tunnel junction, *Nature* 613(7944), 485 (2023) https://doi.org/10.1038/s41586-022-05461-y

32. D. F. Shao, Y. Y. Jiang, J. Ding, S. H. Zhang, Z. A. Wang, R. C. Xiao, G. Gurung, W. J. Lu, Y. P. Sun, and E. Y. Tsymbal, Néel spin currents in antiferromagnets, *Phys. Rev. Lett.* 130(21), 216702 (2023) https://doi.org/10.1103/PhysRevLett.130.216702

33. Y. Y. Jiang, Z. A. Wang, K. Samanta, S. H. Zhang, R. C. Xiao, W. J. Lu, Y. P. Sun, E. Y. Tsymbal, and D. F. Shao, Prediction of giant tunneling magnetoresistance in $RuO_2/TiO_2/RuO_2$ (110) antiferromagnetic tunnel junctions, *Phys. Rev. B* 108(17), 174439 (2023) https://doi.org/10.1103/PhysRevB.108.174439

34. F. Liu, Z. Zhang, X. Yuan, Y. Liu, S. Zhu, Z. Lu, and R. Xiong, Giant tunneling magnetoresistance in insulated altermagnet/ferromagnet junctions induced by spin-dependent tunneling effect, *Phys. Rev. B* 110(13), 134437 (2024) https://doi.org/10.1103/PhysRevB.110.134437

35. B. Chi, L. Jiang, Y. Zhu, G. Yu, C. Wan, and X. Han, Anisotropic spin filtering by an altermagnetic barrier in magnetic tunnel junctions, *Phys. Rev. Appl.* 23(1), 014013 (2025) https://doi.org/10.1103/PhysRevApplied.23.014013

36. L. Zhang, G. Ni, J. He, and G. Gao, Above room temperature multiferroic tunnel junction with the altermagnetic metal CrSb, *Phys. Rev. B* 112(6), 064401 (2025) https://doi.org/10.1103/j559-slg4

37. X. Li, M. Zhu, J. Dong, K. Wu, F. Zheng, and J. Zhang, Tunneling magnetoresistance effect in altermagnetic tunnel junctions with *g*-wave splitting, *Chin. Phys. Lett.* 42(10), 100701 (2025) https://doi.org/10.1088/0256-307X/42/10/100701

38. Y. Shi, G. Zhan, L. Xu, K. Luo, J. Liu, Z. Wu, and H. Liu, Spin-dependent transport in altermagnet CrSb-based magnetic tunnel junction, *Appl. Phys. Lett.* 127(18), 182409 (2025) https://doi.org/10.1063/5.0278985

39. S. Noh, G. H. Kim, J. Lee, H. Jung, U. Seo, G. So, J. Lee, S. Lee, M. Park, S. Yang, Y. S. Oh, H. Jin, C. Sohn, and J. W. Yoo, Tunneling magnetoresistance in altermagnetic RuO_2-based magnetic tunnel junctions, *Phys. Rev. Lett.* 134(24), 246703 (2025) https://doi.org/10.1103/nrk5-5zrj

40. K. Samanta, Y. Y. Jiang, T. R. Paudel, D. F. Shao, and E. Y. Tsymbal, Tunneling magnetoresistance in magnetic tunnel junctions with a single ferromagnetic electrode, *Phys. Rev. B* 109(17), 174407 (2024) https://doi.org/10.1103/PhysRevB.109.174407

41. Y. Zhu, S. Liu, Q. Cui, J. Jiang, H. Yang, T. Zhou, and B. Liu, Tunneling magnetoresistance in altermagnetic tunnel junctions with the half-metal electrode, *Appl. Phys. Lett.* 127(8), 082401 (2025) https://doi.org/10.1063/5.0283614

42. Q. Cui, Y. Zhu, X. Yao, P. Cui, and H. Yang, Giant spin-Hall and tunneling magnetoresistance effects based on a two-dimensional nonrelativistic antiferromagnetic metal, *Phys. Rev. B* 108(2), 024410 (2023) https://doi.org/10.1103/PhysRevB.108.024410

43. L. Zhang, G. Ni, X. Wu, and G. Gao, All-altermagnetic tunnel junction of $RuO_2/NiF_2/RuO_2$, *Chin. Phys. Lett.* 43(4), 040711 (2026) https://doi.org/10.1088/0256-307X/43/4/040711

44. G. Kresse and J. Furthmüller, Efficient iterative schemes for ab initio total-energy calculations using a plane-wave basis set, *Phys. Rev. B* 54(16), 11169 (1996) https://doi.org/10.1103/PhysRevB.54.11169

45. J. P. Perdew, K. Burke, and M. Ernzerhof, Generalized gradient approximation made simple, *Phys. Rev. Lett.* 77(18), 3865 (1996) https://doi.org/10.1103/PhysRevLett.77.3865

46. F. Aryasetiawan, K. Karlsson, O. Jepsen, and U. Schönberger, Calculations of Hubbard *U* from first-principles, *Phys. Rev. B* 74(12), 125106 (2006) https://doi.org/10.1103/PhysRevB.74.125106

47. J. A. Barreda-Argüeso, S. López-Moreno, M. N. Sanz-Ortiz, F. Aguado, R. Valiente, J. González, F. Rodríguez, A. H. Romero, A. Muñoz, L. Nataf, and F. Baudelet, Pressure-induced phase-transition sequence in CoF_2: An experimental and first-principles study on the crystal, vibrational, and electronic properties, *Phys. Rev. B* 88(21), 214108 (2013) https://doi.org/10.1103/PhysRevB.88.214108

48. J. Strempfer, U. Rütt, and W. Jauch, Absolute spin magnetic moment of fef_2 from high energy photon diffraction, *Phys. Rev. Lett.* 86(14), 3152 (2001) https://doi.org/10.1103/PhysRevLett.86.3152

49. A. A. Bolzan, C. Fong, B. J. Kennedy, and C. J. Howard, Structural studies of rutile-type metal dioxides, *Acta Crystallogr. B* 53(3), 373 (1997) https://doi.org/10.1107/S0108768197001468

50. J. Taylor, H. Guo, and J. Wang, Ab initio modeling of quantum transport properties of molecular electronic devices, *Phys. Rev. B* 63(24), 245407 (2001) https://doi.org/10.1103/PhysRevB.63.245407

51. S. L. Dudarev, G. A. Botton, S. Y. Savrasov, C. J. Humphreys, and A. P. Sutton, Electron-energy-loss spectra and the structural stability of nickel oxide: An LSDA+*U* study, *Phys. Rev. B* 57(3), 1505 (1998) https://doi.org/10.1103/PhysRevB.57.1505

52. J. Kang, J. Ryu, J. G. Choi, T. Lee, J. Park, S. Lee, H. Jang, Y. S. Jung, K. J. Kim, and B. G. Park, Current-induced manipulation of exchange bias in IrMn/NiFe bilayer structures, *Nat. Commun.* 12(1), 6420 (2021) https://doi.org/10.1038/s41467-021-26678-x

53. P. Zhang, C. T. Chou, H. Yun, B. C. McGoldrick, J. T. Hou, K. A. Mkhoyan, and L. Liu, Control of Néel vector with spin-orbit torques in an antiferromagnetic insulator with tilted easy plane, *Phys. Rev. Lett.* 129(1), 017203 (2022) https://doi.org/10.1103/PhysRevLett.129.017203

54. C. Pellet-Mary, D. Dutta, M. A. Tschudin, P. Siegwolf, B. Gross, D. A. Broadway, J. Cox, C. Schrader, J. Happacher, D. G. Chica, C. R. Dean, X. Roy, and P. Maletinsky, Lateral exchange bias for Néel-vector control in atomically thin antiferromagnets, *Nat. Commun.* 16(1), 9725 (2025) https://doi.org/10.1038/s41467-025-64700-8

55. Z. Yamani, Z. Tun, and D. H. Ryan, Neutron scattering study of the classical antiferromagnet MnF_2: A perfect hands-on neutron scattering teaching course, *Can. J. Phys.* 88(10), 771 (2010) https://doi.org/10.1139/P10-081

56. W. Jauch, M. Reehuis, and A. J. Schultz, γ-ray and neutron diffraction studies of CoF_2: Magnetostriction, electron density and magnetic moments, *Acta Crystallogr. A* 60(1), 51 (2004) https://doi.org/10.1107/S0108767303022803

57. R. Santos-Ortiz, V. Volkov, S. Schmid, F. L. Kuo, K. Kisslinger, S. Nag, R. Banerjee, Y. Zhu, and N. D. Shepherd, Microstructure and electronic band structure of pulsed laser deposited iron fluoride thin film for battery electrodes, *ACS Appl. Mater. Interfaces* 5(7), 2387 (2013) https://doi.org/10.1021/am3017569

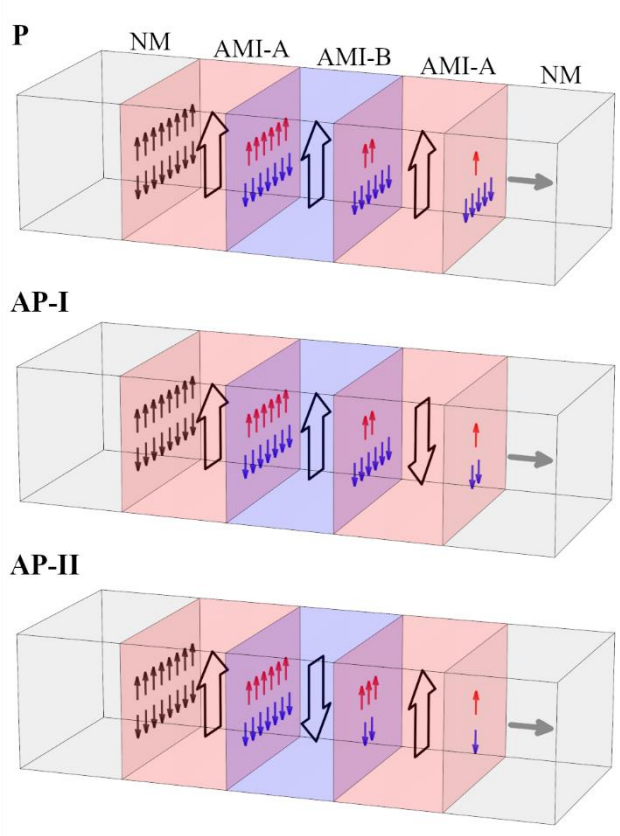

Fig. 1 Schematic illustration of an altermagnetic tunnel junction (AMTJ) with three magnetic configurations. The light-gray cubic regions denote the nonmagnetic metallic electrodes, while the light-pink and light-blue cubes represent the altermagnetic insulating layers (AMI-A and AMI-B) forming the tunnel barrier. Red and blue arrows indicate the tunneling probabilities of the spin-up and spin-down channels, respectively. Black hollow arrows denote the Néel vector orientations in each barrier layer.

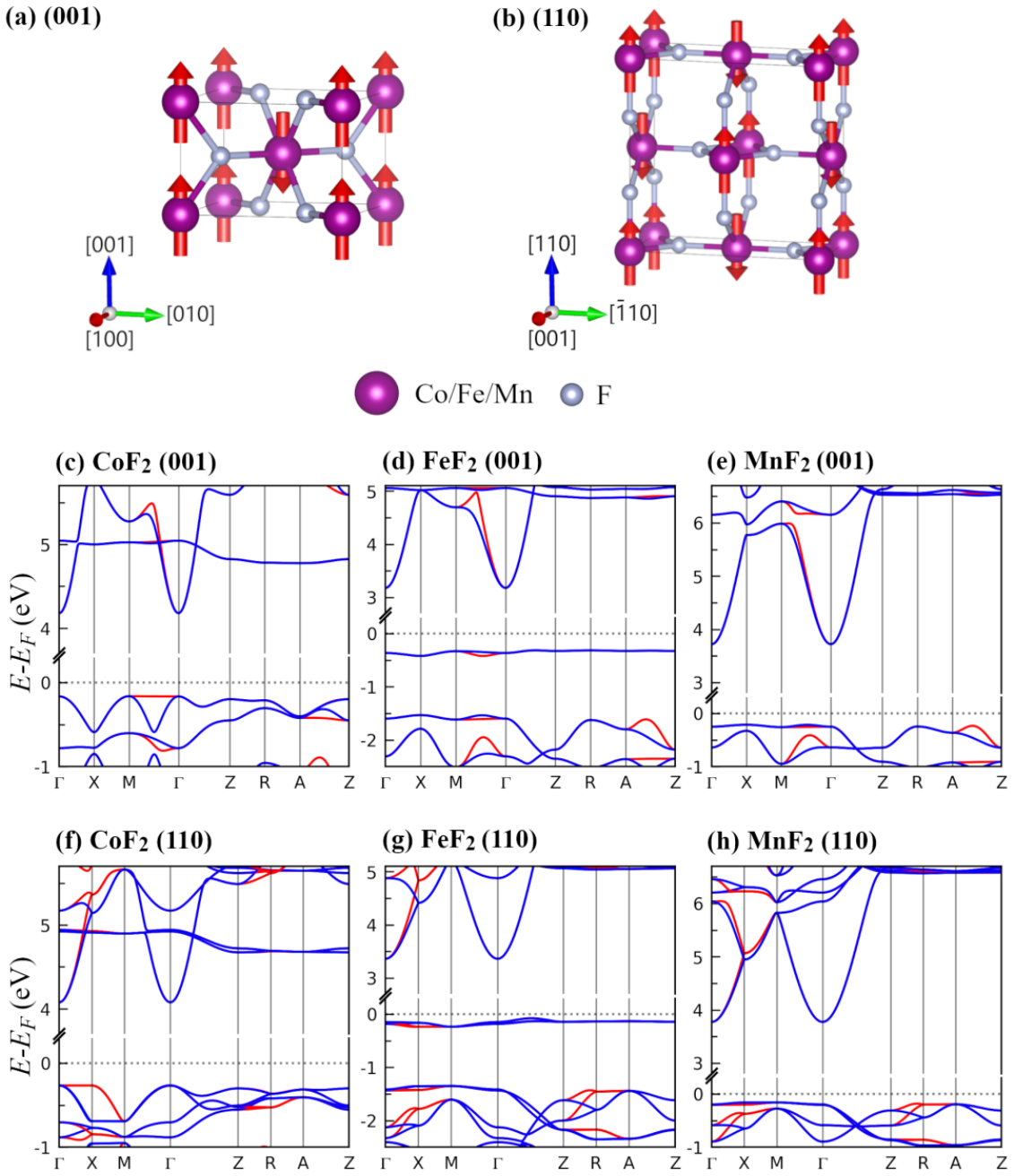

Fig. 2 Atomic and magnetic structures of bulk rutile MF_2 (M = Co, Fe, Mn) for the (001) (a) and (110) (b) faces, respectively. (c–e) Band structures of CoF_2(001), FeF_2(001), and MnF_2(001). (f–h) Band structures of CoF_2(110), FeF_2(110), and MnF_2(110). All band structures are calculated without spin–orbit coupling; red and blue curves denote the spin-up and spin-down channels, respectively.

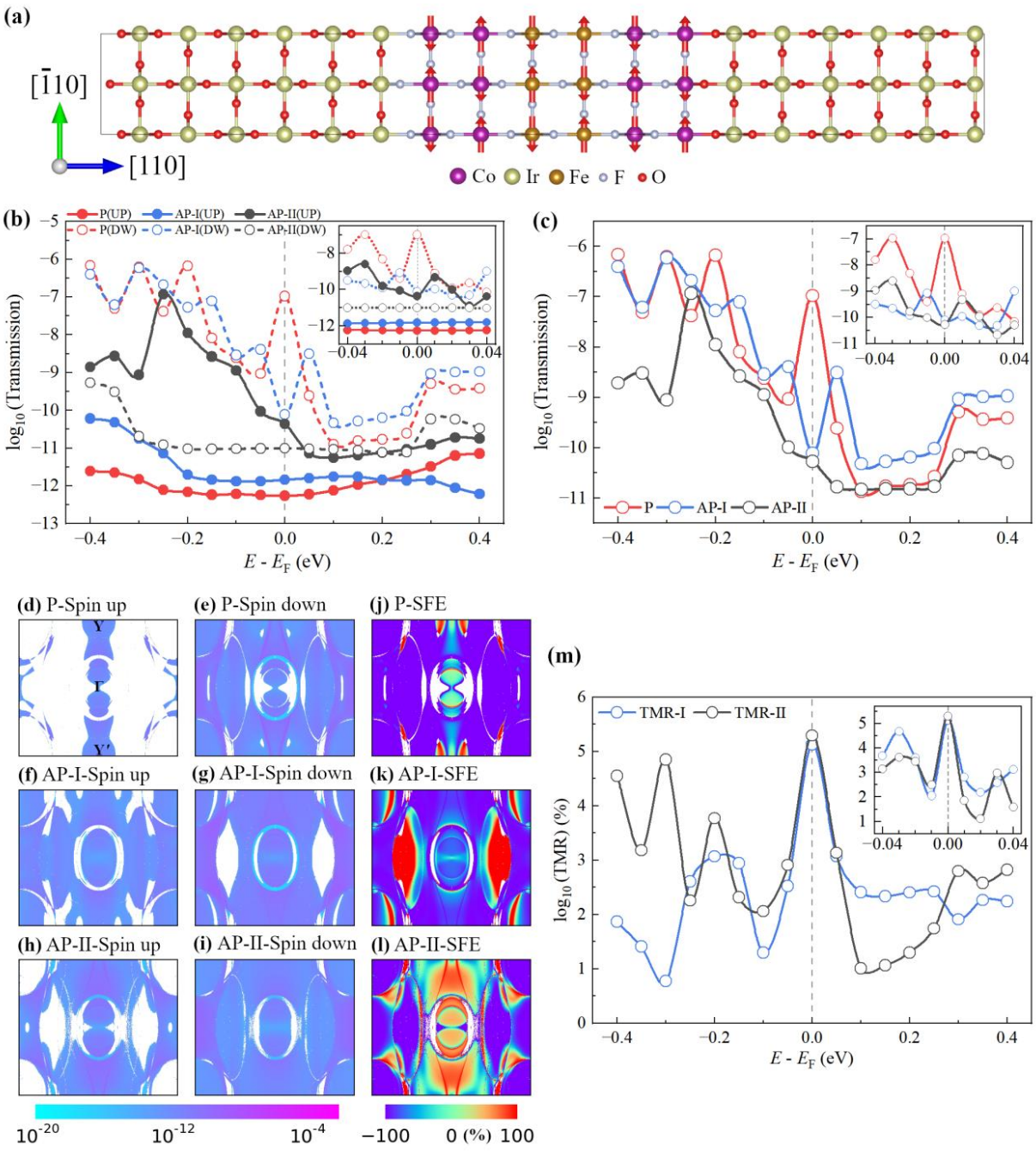

Fig. 3 (a) Atomic structure of the IrO_2(110)/CoF_2/FeF_2/CoF_2/IrO_2 AMTJ. (b) Spin-resolved transmission coefficients as a function of energy. (c) Total transmission coefficients as a function of energy. $\vec{k}_{||}$-resolved transmission spectra in the two-dimensional Brillouin zone (d)–(i), and the corresponding spin-filtering efficiency (j)–(l), defined as $SFE(\vec{k}_{||})=(T_{\uparrow}(\vec{k}_{||})-T_{\downarrow}(\vec{k}_{||}))/(T_{\uparrow}(\vec{k}_{||})+T_{\downarrow}(\vec{k}_{||}))\times100\%$. (m) Energy-dependent TMR ratios. The insets in (b), (c), and (m) are magnified views of the energy window from −0.04 to 0.04 eV.

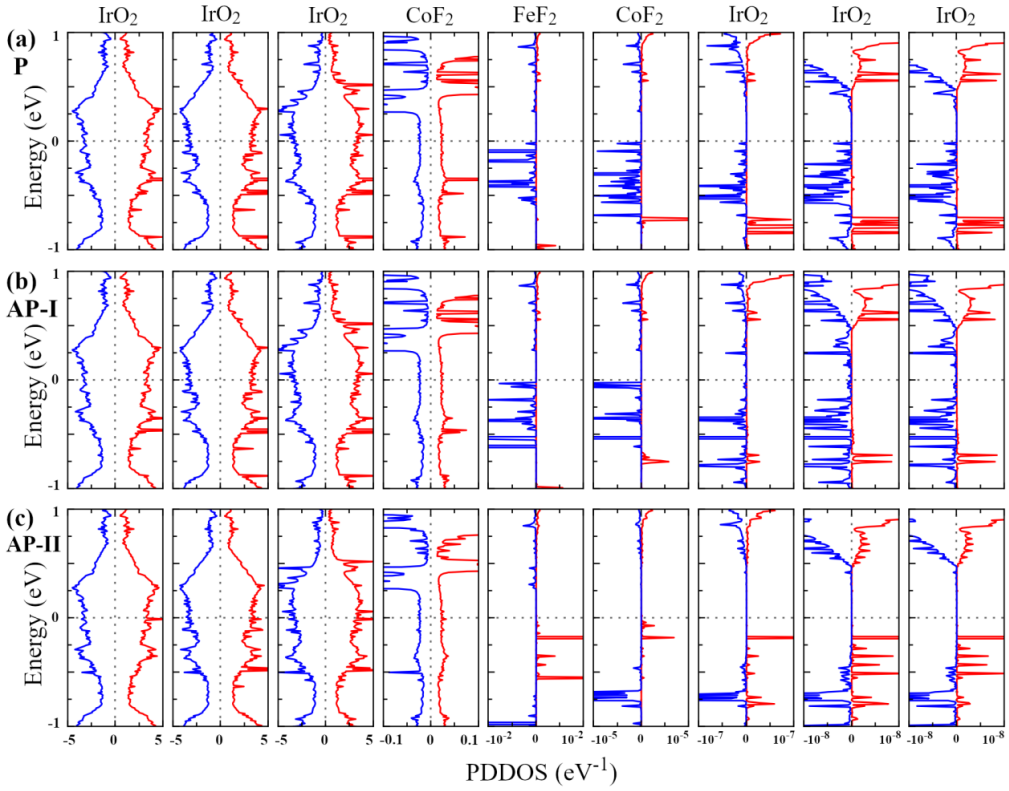

Fig. 4 Spin- and layer-resolved projected device density of states (PDDOS) across the $IrO_2(110)/CoF_2/FeF_2/CoF_2/IrO_2$ AMTJ for the P, AP-I, and AP-II magnetic configurations. Contributions are projected from the left IrO_2 electrode.

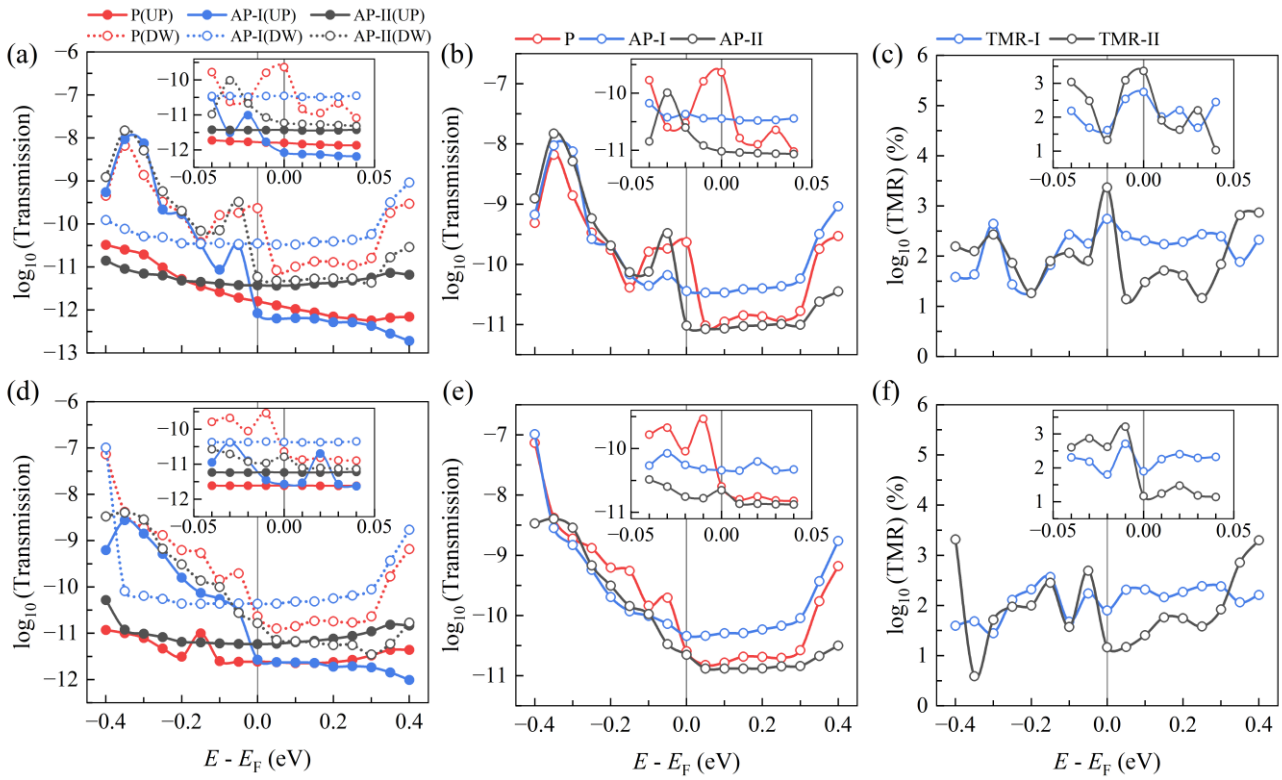

Fig. 5 Spin-resolved transmission coefficients (a) and (d), total transmission coefficients (b) and (e), and TMR ratios (c) and (f) as functions of energy for IrO_2(110)/CoF_2/MnF_2/CoF_2/IrO_2 (a)–(c) and IrO_2(110)/CoF_2/CoF_2/CoF_2/IrO_2 (d)–(f) AMTJs. The insets show magnified views of the energy window from −0.04 to 0.04 eV.